CHAPTER 4

RESULTS AND DISCUSSION

In the present numerical simulation of the impinging jet flow, computation is carried out mainly for the injection pipe diameter of 10.0 and 20.0 mm are used. The jet-to-disk separation distance H is fixed at 10.0, 15.0 and 20.0 mm with the jet flow rate Q_j ranging from 0 to 10.0 slpm and the temperature difference between the bottom and top disks varying from 0 to 40℃. The dimensionless groups governing the flow patterns are the jet Reynolds number and Rayleigh number. They are respectively defined as

$$\mathrm{Re}_j = \overline{V}_j D_j / \nu = 4Q_j / \pi \nu D_j \tag{4.1}$$

and

$$\mathrm{Ra} = g\beta\Delta T H^3 / \alpha\nu \tag{4.2}$$

Thus the corresponding jet Reynolds number ranges from 135 to 1, 352 and the Rayleigh number varies from 0 to 12, 684. Selected results from the present computation are presented here to unravel how the jet Reynolds number, Rayleigh number, and jet-to-disk separation distance affect the vortex flow patterns driven by the interaction of inertia and buoyancy forces in the confined jet impinging flow. It should be mentioned that only the results at steady or statistical state will be examined to investigate the long time behavior of the flow.

4.1 Inertia-Driven Vortex Flow Patterns for Unheated Impinging Disk

At first, the predicted steady vortex flow pattern for the case with H = 20.0 mm, D_j = 10.0 mm and Q_j = 5.0 slpm (Re_j = 676) for the impinging disk unheated (Ra = 0) is presented in Figs. 4.1 and 4.2 by showing the side and top views of the flow. Specifically, the predicted velocity vectors on the cross plane at $\theta = 0^\circ$ and 180° and the contours of the vertical velocity component w on the two horizontal planes at z = -10 and -15 mm are shown. The results clearly show that two regular circular rolls are induced by the impinging jet flow. The inner large one is the primary inertia-driven roll and the outer small one is the secondary inertia-driven roll, both are torus-shaped axisymmetric rolls [2]. The inner circular vortex roll is induced by the entrainment of the air jet injected into the chamber and the secondary roll is in close contact with the primary roll and they are contour-rotating. Examining the velocity vectors at selected time steps during the initial transient reveals that the primary roll is formed immediately after the jet impinging onto the disk. The secondary roll is induced by the viscous shearing effects of the stronger primary roll.

The predicted vortex flow patterns at steady state for various jet Reynolds numbers are shown in Figs. 4.3-4.6 by showing the steady velocity vectors at the cross plane $\theta = 0^\circ$ and 180° for different H and D_j for Ra = 0. The results indicate that the vortex flow is also in the form of circular rolls and the size and intensity of the rolls increase with the jet flow rates. Besides, at certain high Re_j the secondary roll appears. Moreover, at the same Q_j the secondary roll is weaker for a larger injection pipe (D_j = 20.0 mm). Then, the effects of the injection pipe diameter on the impinging jet flow are illustrated in Figs. 4.7 and 4.8 respectively for H = 10.0 and 20.0 mm for Ra = 0. The results manifest that at the same Q_j the jet Reynolds number is higher for the

small injection pipe and thus the resulting vortex rolls are bigger and stronger. Finally, the effects of the jet-to-disk separation distance on the vortex flow are shown in Fig. 4.9. Note that an increase of H from 10.0 mm to 20.0 mm results in a large increase in the size and intensity of the vortex rolls. Note that the smaller primary and secondary inertia-driven rolls at the shorter jet-to-disk separation distance is attributed to the smaller available space between two parallel disks for the rolls to develop at the smaller H. The above results for the characteristics of the inertia-driven rolls are in qualitative agreement with our previous findings for an impinging jet confined in a cylindrical chamber [2, 4].

4.2 Buoyancy-Driven Vortex Flow Patterns for Heated Impinging Disk

In an air jet impinging onto a horizontal heated 8-inch disk confined in a cylindrical chamber, Hsieh et al. [2] observed a buoyancy-induced circular vortex roll prevailed above the outer edge of the disk, aside from the inertia-driven rolls. The typical regular vortex flow pattern in their study is shown in Fig. 4.10 for comparison. There are three steady circular rolls in chamber. The primary inertia-driven circular roll appears in the inner region surrounding the downward air jet. Besides, the smaller secondary inertia-driven roll is induced by the primary inertia-driven roll and appears in the middle zone of the chamber. Specifically, the roll is induced through the viscous shearing effects produced by the stronger and larger inner primary inertia-driven roll, as mentioned in section 4.1. Moreover, the big flow recirculation near the sidewall of the chamber is the buoyancy-driven roll. The inertia-driven rolls are normally stronger and larger at increasing jet Reynolds number.

It is of interest to compare the predicted buoyancy-driven vortex flow from the present computation with that observed by Hsieh et al. [2]. For better comparison, the numerically predicted vortex flow pattern in this study for a case with the same D_j, H, Q_j, Re_j and Ra as those for Fig. 4.10 is shown in Fig. 4.11. The results clearly indicate that in the study of Hsieh [2] the vortex flow is regular. But in the present study for a much larger heated disk the vortex flow is somewhat irregular and the rolls are curved and highly deformed. Besides, there are many buoyancy-driven rolls induced in the space between the horizontal disks and the flow does not reach a steady state at long time. The rolls can be short. Effects of the three parameters Re_j, Ra and H on the vortex flow pattern are examined in the following sections.

4.3 Effects of Jet Reynolds Number

How the jet Reynolds number affects the vortex flow pattern for the impinging jet studied here is shown in Figs. 4.12- 4.16 by displaying the velocity vectors on the cross plane $\theta = 0^\circ$ & 180° for various Ra at H = 10.0 mm. First, for the low temperature difference between the two parallel disk with $\Delta T = 5.0℃$ (Ra = 470), no buoyancy induced secondary flow appears in the jet flow for all Q_j considered (Fig. 4.12 and 4.17). The flow pattern is at steady state and resembles that for the cases with the unheated disk displayed in Fig. 4.3. As ΔT is raised to 10℃ (Ra = 940) the buoyancy in the flow is still low and the buoyancy induced vortex flow is relatively weak and can be barely seen (Figs. 4.13 and 4.18). For a further increase of ΔT to 15 ℃ and at the low Q_j of 1.0 and 2.0 slpm the buoyancy-to-inertia ratios are high enough to induce buoyancy rolls in the outer portion of the chamber (Figs. 4.14 (a) & (b) and 4.19 (a) & (b)). It is noted from the result in Fig 4.19 (a) that at Q_j = 1.0 slpm

the buoyancy-driven rolls are somewhat deformed. But at Q_j = 2.0 slpm regular buoyancy rolls prevail. For a further increase of ΔT to 20 ℃ the buoyancy-driven circular vortex rolls appear for all cases examined here, as evident form the results in Figs. 4.15 and 4.20. More buoyancy rolls are induced at lower Q_j. Again at Q_j = 1.0 slpm the buoyancy rolls deform to a certain degree. This trend continues at an even higher ΔT of 25℃ (Figs. 4.16 and 4.21). Besides, at this higher ΔT deformed buoyancy rolls are seen at Q_j = 1.0 and 2.0 slpm (Figs. 4.21 (a) & (b)). Finally, it is noted from Fig 4.22 that the results from the present computation are in good agreement with those experimental flow visualization by Hsieh [36] for the same configuration of the confined impinging jet. Note that only inertia-driven rolls appear in the flow. A close inspection of the results in Fig. 4.22 revealts that the secondary inertia-driven roll is seen in the experiment but it is not predicted in the numerical simulation. Besides, the primary inertia-driven roll predicted from the computation is larger than that observed in the experiment.

As the jet-to-disk separation distance H is increased to 15.0 mm, the buoyancy-driven vortex flow is expected to be much stronger since the Rayleigh number is proportional to H^3 (Equation (4.2)). The effects of the jet Reynolds number on the vortex flow for H = 15.0 mm at various ΔT are shown in Figs 4.23- 4.30. Note that at this higher H the buoyancy-driven vortex flow deforms significantly even for Q_j = 5.0 slpm and ΔT = 5℃ (Fig. 4.26 (e)). Besides, the flow does not reach steady state at long time according to the time records of radial velocity component u and air temperature given in Figs 4.31- 4.33. Note that the flow is nonperiodic for these cases.

4.4 Effects of Rayliegh Number

We proceed to illustrate how the vortex flow pattern is affected by the Rayleigh number by showing the predicted results for various ΔT at given Q_j. According to the results shown in Figs. 4.34- 4.39 for H = 10.0 mm, at low ΔT of 5℃ no buoyancy-driven vortex roll is induced. But at ΔT = 10℃ and 15℃ a weak buoyancy-driven flow is seen near the outer edge of the heated disk (Figs. 4.34 (b) & (c)). For higher ΔT of 20℃ and 30℃ the buoyancy rolls dominate in the chamber except near the jet axis where the inertia-driven rolls prevail (Figs. 4.34 (d) & (e)). It is of interest to note that at low Q_j and ΔT the weak vortex rolls can be somewhat irregular (Figs. 4.37 (c) & (d)).

It is further illustrated in Figs. 4.40- 4.45 that for the larger H of 15.0 mm the resulting vortex flow is relatively irregular and unsteady at long time especially at a high Ra. The deformation and bifurcation of the rolls are clearly seen from contour plots in Figs. 4.43- 4.45.

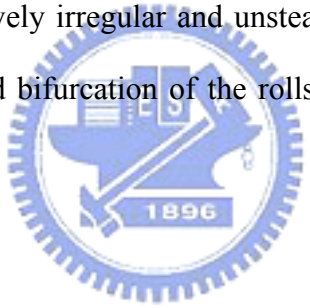

4.5 Effects of Jet-to-Disk Separation Distance

In addition to the physical parameters including the Reynolds and Rayleigh numbers, the above results already show that the jet-to-disk separation distance can significantly affect the vortex flow pattern in the chamber. This is the direct consequence of the simple fact that at given Q_j and ΔT the Rayleigh number Ra is proportional to the third power of the jet-to-disk separation distance H (Eq. (4.2)). To further illustrate the effects of the jet-to-disk separation distance, the predicted results for the same Q_j and ΔT but different H are shown together in Figs. 4.46- 4.51. The results clearly indicate that when H is increased from 10.0 mm to 15.0 mm the vortex flow changes from a rather regular pattern to a highly irregular state. For several cases,

no buoyancy-driven roll appears in the chamber for H = 10.0 mm. But for H = 15.0 mm the buoyancy-driven vortex flow is irregular and unsteady.

4.6 New Flow Patterns at High Jet Reynolds Numbers

The results presented above show that in the air jet impinging onto a large heated disk the deformation, termination and splitting of the circular vortex rolls tend to appear at high Reynolds numbers. A close inspection of the results for Q_j = 5.0 slpm given in Fig. 4.45 suggests that in the inner region dominated by the primary inertia-driven roll this roll may have split into several short radial rolls at high jet Reynolds number under the action of the upward buoyancy force due to the heated disk (Fig. 4.45 (c)). These radial rolls can also be regarded as deformed vortices. To explore the presence of the radial rolls, computations are performed for the cases with higher Q_j. The results from these computations are shown in Figs. 4.52 and 4.53. Note that for Q_j = 10 slpm (Re_j = 1, 352) and ΔT = 10.0 ℃ short radial rolls do appear in the impinging region around the jet axis (Fig. 4.53 (c)). More computations are needed to fully insure the presence of the radial rolls.

4.7 Flow Regime Map

Based on the results obtained in the present study, a flow regime map for the cases with H = 10.0 mm delineating three different buoyancy-driven vortex flow patterns in the mixed convection confined impinging jet is shown in Fig. 4.54. The results in this plot manifest that at high buoyancy-to-inertia ratio Gr/Re_j^2 the

buoyancy-driven vortex rolls become irregular. Then for the larger jet-to-disk separation distance with H = 15.0 mm the driven vortex flow is unsteady and irregular for the low jet Reynolds numbers. While at low Gr/Re_j^2 the flow becomes regular and is in the form of circular rolls. At even lower Gr/Re_j^2 no buoyancy-driven vortex roll appears. It is of interest to study the patterns of the inertia-driven rolls. This is given in Fig. 4.55. Note that at low Re_j with the disk heated the inertia-driven rolls are irregular. At higher Re_j the rolls are regularized. Note that at high Re_j and with Ra exceeding certain critical level we have short radial rolls in the flow.

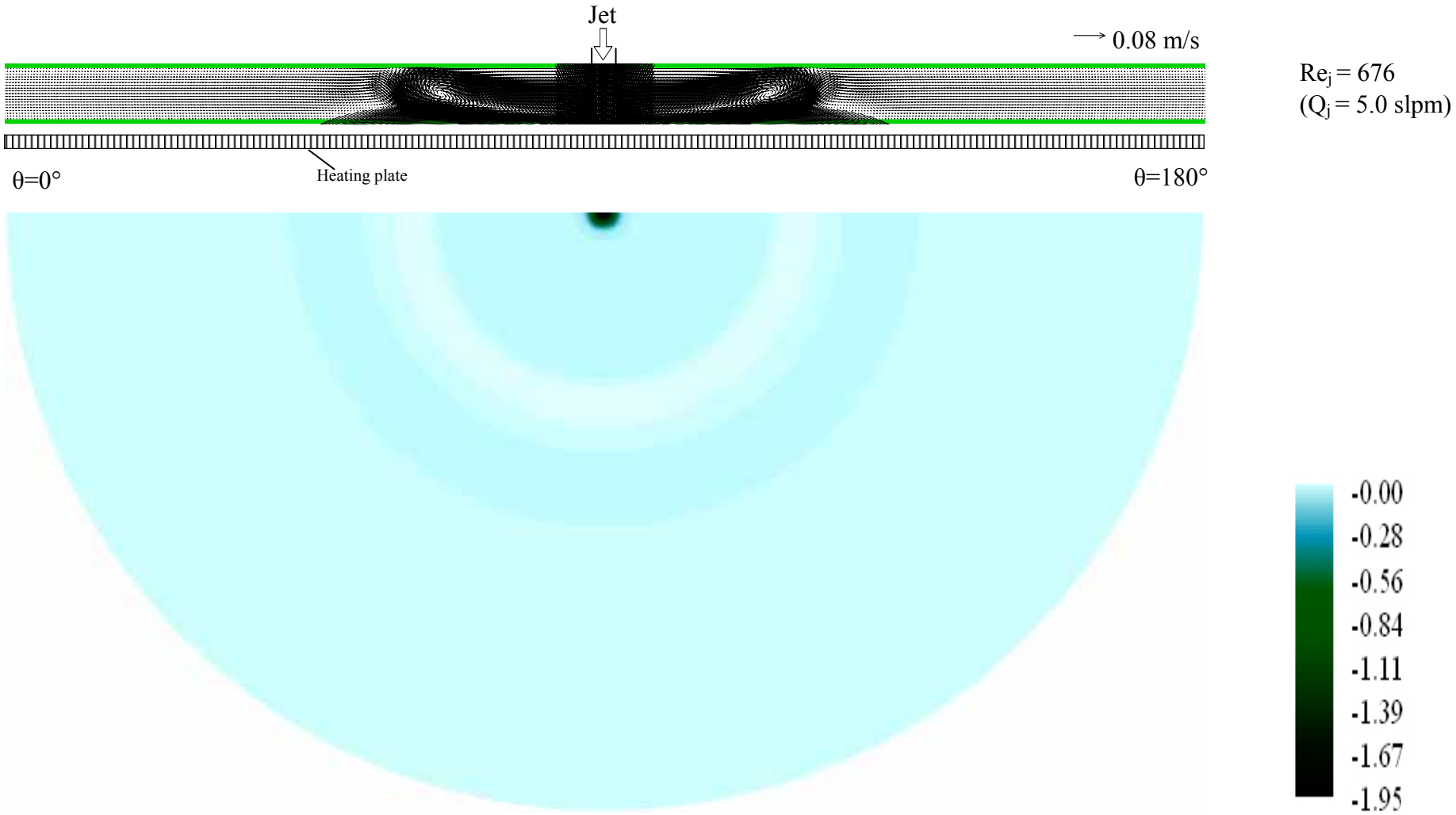

Fig. 4.1 Steady vortex flow for D_j = 10.0 mm, H = 20.0 mm, and Ra = 0 ($\Delta T = 0℃$) at Re_j = 676 (Q_j = 5.0 slpm): (a) velocity vectors on the vertical plane θ= 0° & 180° and (b) contours of w at the horizontal plane z = -10.0 mm.

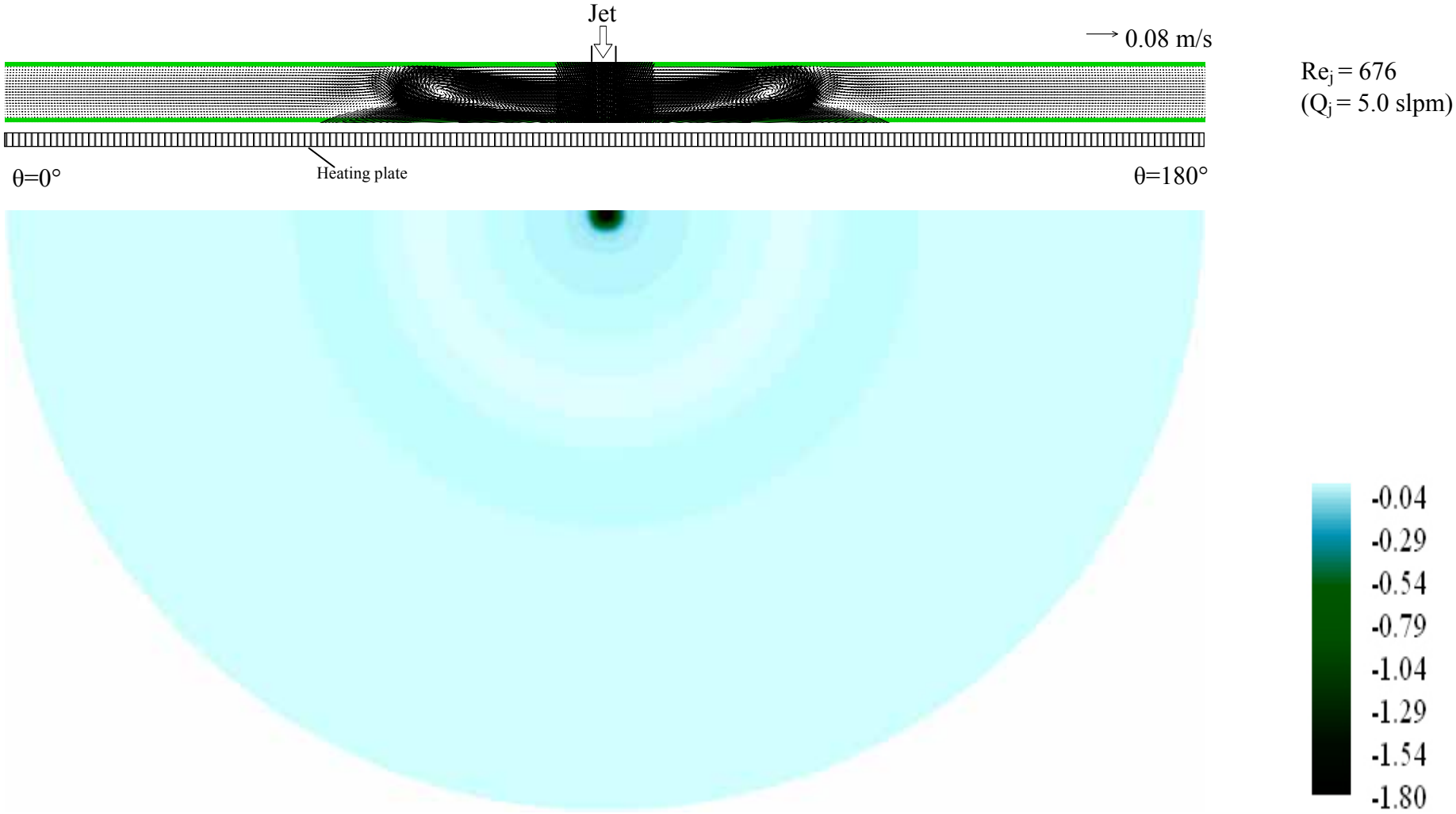

Fig. 4.2 Steady vortex flow for D_j = 10.0 mm, H = 20.0 mm, and Ra = 0 ($\Delta T = 0℃$) at Re_j = 676 (Q_j = 5.0 slpm): (a) velocity vectors on the vertical plane θ= 0° & 180° and (b) contours of w at the horizontal plane z = -15.0 mm.